

PROCEEDINGS OF SPIE

SPIDigitalLibrary.org/conference-proceedings-of-spie

Visualization of custom drill bit tips in a human vertebra for photoacoustic-guided spinal fusion surgeries

Eduardo Gonzalez, Alycen Wiacek, Muyinatu A. Lediju Bell

Eduardo Gonzalez, Alycen Wiacek, Muyinatu A. Lediju Bell, "Visualization of custom drill bit tips in a human vertebra for photoacoustic-guided spinal fusion surgeries," Proc. SPIE 10878, Photons Plus Ultrasound: Imaging and Sensing 2019, 108785M (27 February 2019); doi: 10.1117/12.2510688

SPIE.

Event: SPIE BiOS, 2019, San Francisco, California, United States

Visualization of custom drill bit tips in a human vertebra for photoacoustic-guided spinal fusion surgeries

Eduardo Gonzalez^a, Alycen Wiacek^b, and Muyinatu A. Lediju Bell^{a,b,c}

^aDepartment of Biomedical Engineering, Johns Hopkins University, Baltimore, MD, USA

^bDepartment of Electrical and Computer Engineering, Johns Hopkins University, Baltimore, MD, USA

^cDepartment of Computer Science, Johns Hopkins University, Baltimore, MD, USA

ABSTRACT

Spinal fusion surgeries require the insertion of screws into the pedicles of vertebrae in order to connect multiple vertebrae with a metal rod and stabilize the spine after an injury. When performing this procedure, it is critical to ensure that a drill tip maintains the correct trajectory, which will prevent bone breaches when drilling pilot holes for screw insertion. In this work, we demonstrate a photoacoustic imaging system for drill tip tracking that will co-register photoacoustic images with pre-operative CT images. Our approach was tested with two custom drill bits, each containing a hollow core with either a single hole or multiple holes located at the drill bit tip. An optical fiber was inserted in the core of each drill bit to enable light delivery to the drill bit tip. The custom drill bits were then inserted into the pedicle of an *ex vivo* human vertebra containing a 32 mm-deep pre-drilled hole. The the first 13 mm of the pre-drilled hole corresponded to the depth of the pedicle and the remaining 19 mm extended into the vertebral body. Data were acquired using a 760 nm laser with energies of 1.0 mJ, 2.2 mJ, and 3.4 mJ at the fiber tip. With the single-hole drill bit tip, photoacoustic signals were detectable at 0-6 mm insertion depths into the pedicle with up to 53.7 SNR. At insertion depths of 6 mm to 14 mm, the photoacoustic signal was either no longer visualized or shifted from its expected location in the image due to reflection artifacts. SNR was improved with coherence-based beamforming methods when compared to conventional delay-and-sum beamforming methods, particularly when imaging with lower laser energies. Results are generally promising for photoacoustic-guided drilling during pedicle screw insertion.

1. INTRODUCTION

Spinal deformities can be caused by degenerative disorders, trauma, and primary or metastatic cancer.¹ Such abnormalities are often corrected with spinal fusion surgeries, which help to alleviate pain, recover neurological functionality, or repair damaged bone tissue. These surgeries are performed by drilling holes into the pedicles of vertebrae, inserting pedicle screws, and fixing each screw to a metal rod with the ultimate goal of stabilizing the spine to normal function. However, when drilling a hole for screw insertion, it is critical to ensure the correct trajectory during drilling in order to avoid accidental bone breaches and the associated screw misplacement. Pedicle screw misplacement during spinal fusion surgeries occurs in approximately 14–39.8% of procedures.^{2–5}

Image-guided fluoroscopy may be used to provide intraoperative information, which can be registered to preoperative computer tomography (CT) images. The surgical tool and anatomical landmarks are then identified in the registered images to help surgeons localize the drill bit. Limitations of these x-ray-based imaging modalities include poor soft tissue differentiation and ionizing radiation, which can be harmful with repeated exposure. In contrast, ultrasound imaging is a safer alternative, with the potential to provide real-time information. However, ultrasound has limited ability to detect deep-lying features beneath bone tissue due to sound attenuation and sound speed differences.⁶

To overcome the limitations of ultrasound and fluoroscopy, photoacoustic imaging⁷ has been proposed as a guidance method for pedicle screw insertion.⁸ The proposed technique consists of delivering laser light to generate pressure waves. The pressure waves are then received by an ultrasound probe, and beamforming techniques are applied to create a photoacoustic image. Applications of photoacoustic imaging has shown promising results in the visualization of blood vessels,⁹ neurosurgical tools,¹⁰ and discrimination of cortical bone from cancellous bone in a fresh human cadaveric vertebra.⁸

In this paper, we propose a photoacoustic imaging system for drill tip tracking that will co-register photoacoustic images with pre-operative CT image acquisitions. A set of custom drill bits¹¹ adapted to accommodate the insertion of an optical fiber were tested on an *ex vivo* human vertebra at multiple laser energies and insertion depths. In addition, we explored the effects of applying coherence-based beamforming techniques to the received photoacoustic signals.

2. METHODS

2.1 Data Acquisition

A human lumbar vertebra with pre-drilled holes in the pedicles was submerged and fixed in a water tank. A pulsed laser operating at 760 nm wavelength (Phocus Mobile, Oportek Inc., Carlsbad, CA) was coupled to one of two custom hollow drill bits containing a 0.6 mm core diameter optical fiber to deliver light and generate photoacoustic signals. Channel data was acquired with an Alpinion SP1-5 phased array transducer, connected to an Alpinion ECUBE-12R system.

One of the custom drill bits contained a single through hole, as shown in Fig. 1A. The second custom drill bit contained a single through hole that bifurcated into three holes at the drill bit tip, as shown in Fig. 1B. An optical fiber was inserted into the through-hole of each drill bit. These custom drill bit designs were described in our previous publication.¹¹

Tape was adhered to each drill bit and labeled with lines corresponding to 0 mm to 14 mm insertion depths in 2 mm increments (see Figs. 1C and 1D). Photoacoustic imaging was performed with the drill bit inserted into the pedicle up to a marked distance. The laser energy was varied from 1.0 mJ to 2.2 mJ to 3.4 mJ for each distance. A total of 200 frames were acquired for each possible pair of drill bit insertion distance and laser energy.

Ultrasound B-mode images of the *ex vivo* human vertebra were acquired and co-registered with CT data. Given that photoacoustic and ultrasound data are obtained with the same ultrasound transducer, registration of ultrasound-to-CT images simultaneously produces the transformation matrix needed to perform photoacoustic-to-CT image registration. Ultrasound images were acquired with 3.5 MHz center frequency, an image depth of 80 mm, and a focus located at 60 mm depth. CT acquisitions were performed using a SIEMENS ARCADIS Orbic 3D C-Arm with 190 raw projections and 0.23 mm³ voxel resolution. Rigid monomodal registration was conducted using a regular step gradient descent optimizer.¹²

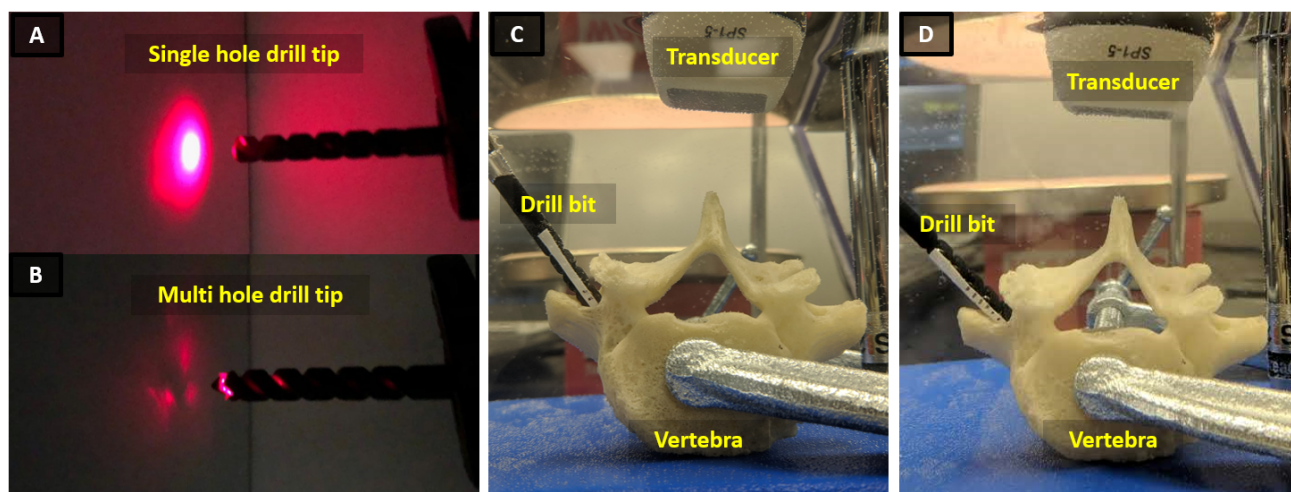


Figure 1: (A) Single-hole drill bit tip. (B) Multi-hole drill bit tip. Tape was adhered to each drill bit and labeled in 2 mm increments from 0 mm to 14 mm. *Ex vivo* setup of the human vertebra submerged in a water tank showing the drill bits entering (C) 10 mm and (D) 2 mm into the pedicle.

2.2 Photoacoustic Beamforming

Four types of beamforming methods were applied to create photoacoustic images of the 200 frames of photoacoustic data acquired with each depth-energy pair described above: (1) conventional delay-and-sum (DAS) beamforming, with data averaged during the delay step; (2) DAS beamforming with images averaged after the DAS beamforming step; (3) Short-Lag Spatial Coherence (SLSC) beamforming;¹³ and (4) Locally Weighted Short Lag Spatial Coherence (LW-SLSC) beamforming.¹² For SLSC and LW-SLSC beamforming, incoherent noise was reduced by averaging the delayed signals over 200 acquisitions after the delay step.

To implement SLSC imaging, a coherence function, \hat{R} , as a function of spatial lag, m , was calculated as:

$$\hat{R}(m) = \frac{1}{N-m} \sum_{i=1}^{N-m} \frac{\sum_{n=n_1}^{n_2} s_i(n) s_{i+m}(n)}{\sqrt{\sum_{n=n_1}^{n_2} s_i^2(n) \sum_{n=n_1}^{n_2} s_{i+m}^2(n)}}, \quad (1)$$

where N is the the number of elements in the aperture, and n_1 and n_2 are the limits of the axial kernel. An SLSC image of cumulative lag M was then generated as the integral of the spatial coherence function over the first M lags:

$$\text{SLSC}(M) = \int_1^M \hat{R}(m) dm \approx \sum_{m=1}^M \hat{R}(m). \quad (2)$$

The chosen M values ranged from $M = 1$ to $M = 50$.

Contrast enhancement of bony ultrasound surfaces was previously achieved by implementing a regularized version of the SLSC beamforming, namely the Locally Weighted Short Lag Spatial Coherence (LW-SLSC).¹² In this study, we hypothesize that photoacoustic signals reconstructed with LW-SLSC will have similarly improved contrast while preserving spatial resolution. The input of this beamformer is the coherence matrix \hat{R} from SLSC beamforming, which is utilized to find the optimized weighted coefficient by minimizing the total variation (TV) of the weighted sum within a moving kernel, as described by the following equation:

$$\hat{w}_i = \text{argmin}\{\text{TV}(w_i \hat{R}_{K_i}) + \alpha \|\nabla w_i\|^2\}, \quad (3)$$

where TV is the total variation, \hat{R}_{K_i} is the kernel i of the correlation matrix \hat{R} , w_i the optimized weight vector for the calculated summed lags of \hat{R}_{K_i} (with dimensions $[1 \times N_L]$, where N_L is the maximum number of cumulative lags that are summed up to a specific M value), and $\|\nabla w_i\|^2$ is the L2-norm of the gradient operator, which is used to preserve high resolution information. LW-SLSC imaging relies on the adaptive selection of lower lags in kernels surrounding regions of similar amplitude and higher lags otherwise, which reduces the noise commonly present in SLSC images created with higher M values. LW-SLSC images were computed with a kernel size of 1.20 mm (lateral) x 1.92 mm (axial), 60% overlap between neighboring kernels, $N_L = 50$, and $\alpha = 1000$.

2.3 Data Analysis

Signal-to-noise ratio (SNR) was evaluated using a background reference located in the vertebral foramen (see Fig. 2C), according to the following equation:^{14,15}

$$\text{SNR} = \frac{\mu_{\text{signal}}}{\text{RMS}_{\text{background}}}, \quad (4)$$

where μ_{signal} is the mean within a pre-defined region of interest (ROI) encompassing the photoacoustic signal and $\text{RMS}_{\text{background}}$ is the root mean square of signals within a ROI that corresponds to the vertebral foramen.

3. RESULTS

Fig. 2 shows examples of photoacoustic beamformed images registered with CT images. Signals corresponding to the drill tip are identified with blue boxes and artifacts are shown with yellow boxes. Fig. 2A, shows DAS photoacoustic images acquired with 2.2 mJ energy with an insertion depth of 6 mm into the pedicle. The multi-hole drill bit tip was utilized to create this image. Fig. 2B shows a LW-SLSC photoacoustic image created from

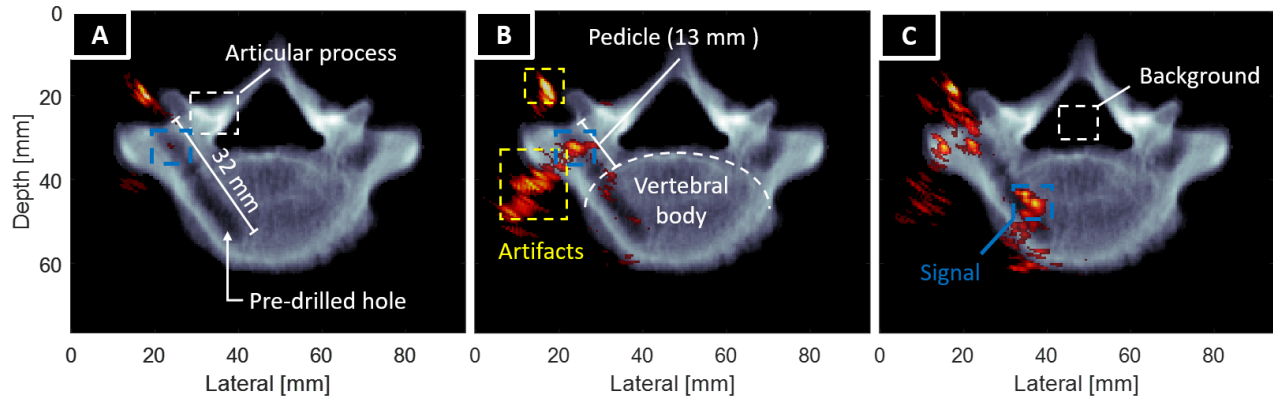


Figure 2: Examples of registered photoacoustic images (red) with CT images (gray). (A) DAS image (averaged after applying time delays) created with the multi-hole drill bit tip, 2.2 mJ energy, and 6 mm insertion depth. (B) LW-SLSC created with the same channel data (multi-hole drill bit tip, 2.2 mJ, 6 mm insertion depth). (C) SLSC ($M = 30$) created with the single-hole drill tip, 3.4 mJ energy, 14 mm insertion depth. Photoacoustic signals are identified with blue boxes. Artifacts are identified with yellow boxes. The white box in (C) indicates the background ROI that was used for contrast measurements.

the same channel data and demonstrates an improvement in the visualization of the photoacoustic image, when compared to the DAS result in Fig. 2A.

Both LW-SLSC and SLSC beamforming enabled the visualization of photoacoustic signals from 0 to 6 mm depth. However, as observed in the LW-SLSC image of Fig. 2B, there was a tail that artifact originated from the photoacoustic signal. At distances of 8 mm and 10 mm into the pedicle, the amplitude of the signal decreased for all reconstructed images. Finally, at insertion depths of 12 mm and 14 mm, reflection artifacts were observed in the vertebral body region, with an example SLSC image shown in Fig. 2C.

Fig. 3 shows the insertion distance measured from photoacoustic images as a function of the known insertion distance. The ideal result is shown as the blue solid line. The measured result was performed by first selecting two fixed points at the drill hole opening on the CT image of the vertebra, then selecting the photoacoustic signal with the highest intensity around the expected location and discarding reflection artifacts located outside of the vertebra. The final distance was obtained by calculating the average of the euclidean distance between the photoacoustic point and each of the CT fixed points. From 0 mm to 8 mm depth, the mean \pm one standard deviation of the position error was 1.02 ± 0.81 mm for multi-hole drill bit tip and 1.50 ± 0.52 mm for the

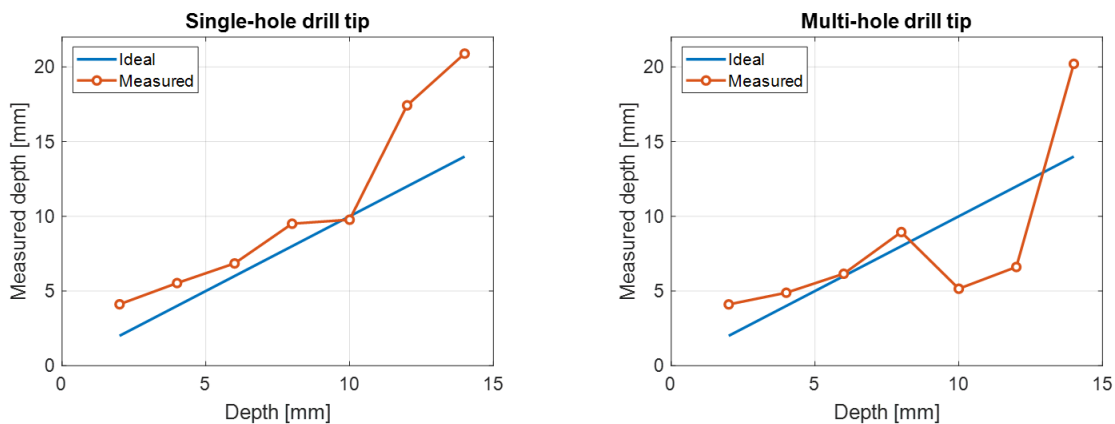


Figure 3: Insertion distance comparison with LW-SLSC photoacoustic images.

single-hole drill bit tip. At depths greater than 8 mm, this error increased to 5.48 ± 6.54 mm for the multi-hole drill bit tip and 4.18 ± 3.76 mm for the single-hole drill bit tip.

Fig. 4 shows the SNR measurements of photoacoustic signals from DAS, SLSC, and LW-SLSC images at multiple insertion depths. Measurements of SNR were based on signals selected for the distance measurements in Fig. 3. Overall, SNR is greatest for all beamformed images created with the higher laser energies. In particular, for the 2 mm to 8 mm insertion distance range, the mean \pm one standard deviation of the measured SNR in LW-SLSC images for all plots shown in Fig. 4 was 41.26 ± 21.76 , 51.24 ± 27.90 , and 53.68 ± 36.81 for energies of 1.0 mJ, 2.2 mJ and 3.4 mJ, respectively. When averaging frames at the delay stage, an SNR improvement of 2.75 ± 1.75 was achieved for the DAS images (when compared to averaging after the beamforming stage). In addition, the mean \pm one standard deviation of the SNR improvements for all plots shown in Fig. 4 was 21.85 ± 11.90 with SLSC imaging (when compared to DAS images created with channel data averaged at the delay stage). Similarly, an SNR improvement of 31.14 ± 23.05 was achieved with LW-SLSC imaging (when compared to DAS images created with channel data averaged at the delay stage). As observed in Fig. 4, the main difference between the single-hole results and the multi-hole results is the decreased signal intensity for all the reconstructed images with the multi-hole drill tip. This likely occurs because energy exits the drill tip with more diffusion than that of the single-hole case, thus generating more reflections that do not converge when delaying the signals across the aperture to account for time of arrival differences.

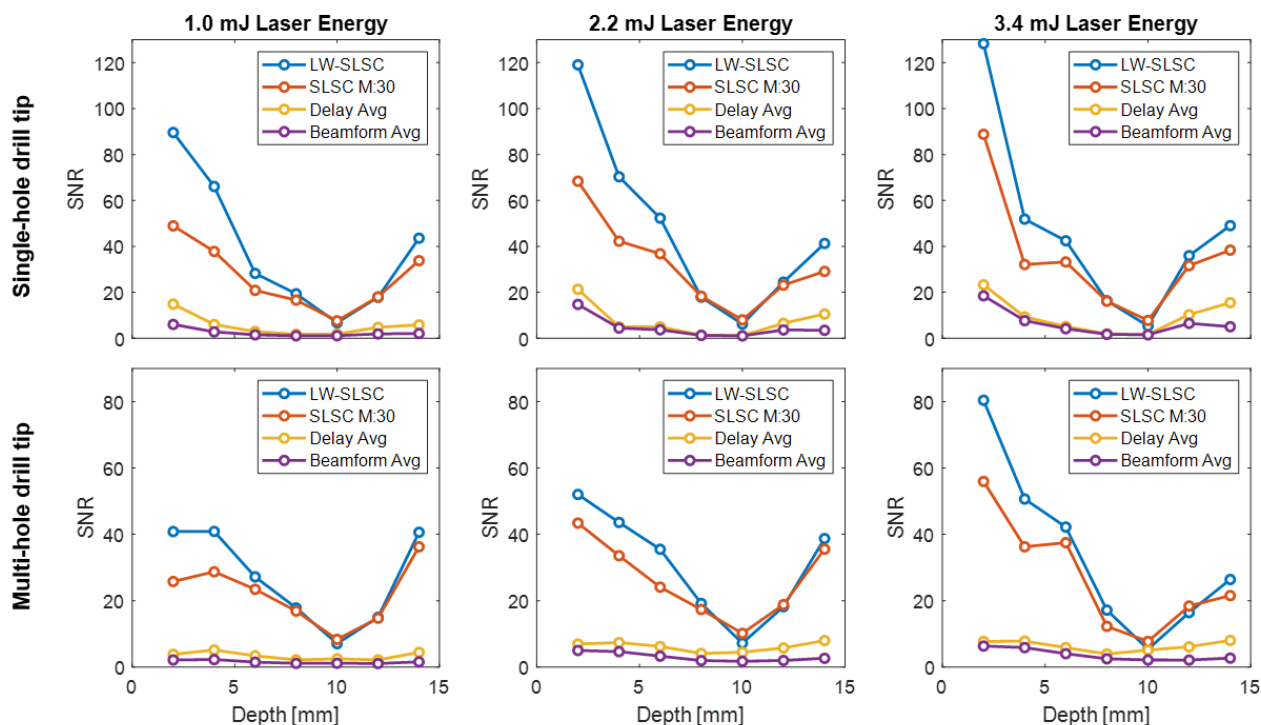


Figure 4: SNR reported as a function of insertion depth into the pedicle for the four photoacoustic beamforming methods described in Section 2.2: DAS with beamformed images averaged; DAS with delayed raw channel data averaged; SLSC images created with $M = 30$; and LW-SLSC images. These results are shown for both the single-hole drill tip (top) and the multi-hole drill tip (bottom) for multiple laser energies.

4. DISCUSSION

This study is the first to evaluate the effects of photoacoustic signals from custom drill bits inserted in the pedicle region of a human vertebra. Results demonstrate the feasibility of tracking the drill tip with photoacoustic image guidance within a 0-6 mm insertion depth range. This range corresponds to 46.15% of the total length of the

pedicle. We have also shown that LW-SLSC and SLSC beamforming outperform conventional DAS beamforming when displaying and visualizing photoacoustic signals inside a drilled hole (see Fig. 4). In particular, from 0 mm to 6 mm insertion depths, LW-SLSC and SLSC significantly enhance SNR at energies as low as 1.0 mJ.

A primary limitation of this approach is the two types of artifacts that were observed in the photoacoustic images. The first artifact appears as a shifted point source (see upper yellow box in Fig. 2B). A potential cause of this artifact is the interaction between the drill shaft exposed to water and the fiber inserted in the hollow core of the drill bit. This fiber appears to have its cladding accidentally removed, which prevented total internal reflection within the drill shaft and causes some leakage of the laser light. This source of artifact could be addressed by taking care to retain the cladding when inserting the fiber into the hollow core of the drill bit. Another cause of this artifact could be reflections from the drill tip that exit the drill hole and travel through the water-only path outside the vertebra and towards the transducer.

The second artifact appears as a tail that originates from the true point source (see lower yellow box in Fig. 2B). For this artifact, the diffuse pattern could be a consequence of phase aberration that is applied to the photoacoustic signal when traveling across the articular process, which is composed of cortical bone (notice the high density of the CT images in Fig. 2A, at the top right region near the entrance of the drill hole). Phase aberration is commonly produced by the heterogeneous sound speed of the medium, which generates errors in the beamforming process, as most beamformers assume a single sound speed value for reconstruction. Coherence-based beamforming methods are beneficial to recover some of the aberrated signals when compared to conventional DAS beamforming. Thus, signals within the drilled hole are better visualized when using SLSC and LW-SLSC beamforming (see Fig. 2B and Fig. 2C) when compared to DAS beamforming (see the signals surrounded by blue boxes in Fig. 2A and Fig. 2B). Future work will explore deep learning approaches to eliminate these reflection artifacts.^{16–18}

A secondary limitation of this approach is that the drill location error increased as distance increased beyond 8–10 mm insertion depth into the pedicle (see Fig. 3). A possible explanation for these larger errors is the sound speed difference between the cancellous bone located in the vertebral body (1918 ± 305 m/s¹⁹) and the water (1480 m/s²⁰).

5. CONCLUSION

Evaluation of photoacoustic signals was conducted at multiple depths within the pedicle and at multiple energies, with custom drill bit tips containing a single and multiple holes for light delivery. For both drill bits, significant SNR improvement was observed with the implementation of coherence-based SLSC and LW-SLSC beamforming methods, when compared to conventional DAS beamforming methods. Results suggest that it is possible to track the drill tip with insertion depths up to 6 mm within a pedicle. The proposed approach to implement photoacoustic-based guidance of pedicle screw insertion with this approach has two limitations. One limitation is the appearance of artifacts, and the second limitation is increased localization and/or tracking errors with increased insertion depth. Despite these limitations, results demonstrate the overall feasibility of photoacoustic-guided drilling for pedicle screw insertion.

6. ACKNOWLEDGMENTS

This work was partially supported by NIH grant R00 EB018994 and a Fulbright Foreign Student Program grant. The authors also acknowledge the support of NVIDIA Corporation with the donation of the Titan Xp GPU used for this research. In addition, the authors thank Gerhard Kleinzig and Sebastian Vogt from Siemens Healthineers for making a Siemens ARCADIS Orbic 3D available.

REFERENCES

- [1] Manbachi, A., Cobbold, R. S., and Ginsberg, H. J., “Guided pedicle screw insertion: techniques and training,” *The Spine Journal* **14**(1), 165–179 (2014).
- [2] Abul-Kasim, K. and Ohlin, A., “The rate of screw misplacement in segmental pedicle screw fixation in adolescent idiopathic scoliosis: The effect of learning and cumulative experience,” *Acta Orthopaedica* **82**(1), 50–55 (2011).

- [3] Gertzbein, S. D. and Robbins, S. E., “Accuracy of pedicular screw placement in vivo.,” *Spine* **15**(1), 11–14 (1990).
- [4] Castro, W. H., Halm, H., Jerosch, J., Malms, J., Steinbeck, J., and Blasius, S., “Accuracy of pedicle screw placement in lumbar vertebrae,” *Spine* **21**(11), 1320–1324 (1996).
- [5] Laine, T., Mäkitalo, K., Schlenzka, D., Tallroth, K., Poussa, M., and Alho, A., “Accuracy of pedicle screw insertion: a prospective ct study in 30 low back patients,” *European Spine Journal* **6**(6), 402–405 (1997).
- [6] Brendel, B., Rick, S. W. A., Stockheim, M., and Ermert, H., “Registration of 3d ct and ultrasound datasets of the spine using bone structures,” *Computer Aided Surgery* **7**(3), 146–155 (2002).
- [7] Beard, P., “Biomedical photoacoustic imaging,” *Interface Focus* **1**(4), 602–631 (2011).
- [8] Shubert, J. and Bell, M. A. L., “Photoacoustic imaging of a human vertebra: implications for guiding spinal fusion surgeries,” *Physics in Medicine and Biology* (2018).
- [9] Kolkman, R. G., Steenbergen, W., and van Leeuwen, T. G., “In vivo photoacoustic imaging of blood vessels with a pulsed laser diode,” *Lasers in Medical Science* **21**(3), 134–139 (2006).
- [10] Eddins, B. and Bell, M. A. L., “Design of a multifiber light delivery system for photoacoustic-guided surgery,” *Journal of Biomedical Optics* **22**(4), 041011 (2017).
- [11] Shubert, J. and Bell, M. A. L., “A novel drill design for photoacoustic guided surgeries,” in [*Photons Plus Ultrasound: Imaging and Sensing 2018*], **10494**, 104940J, International Society for Optics and Photonics (2018).
- [12] Gonzalez, E. and Lediju Bell, M. A., “Segmenting bone structures in ultrasound images with locally weighted slsc (lw-slsc) beamforming,” *IEEE International Ultrasonics Symposium* (2018).
- [13] Lediju, M. A., Trahey, G. E., Byram, B. C., and Dahl, J. J., “Short-lag spatial coherence of backscattered echoes: Imaging characteristics,” *IEEE Transactions on Ultrasonics, Ferroelectrics, and Frequency Control* **58**(7) (2011).
- [14] Bhargava, R. and Levin, I. W., “Fourier transform infrared imaging: theory and practice,” *Analytical Chemistry* **73**(21), 5157–5167 (2001).
- [15] Hayes, C. E., Hattes, N., and Roemer, P. B., “Volume imaging with mr phased arrays,” *Magnetic Resonance in Medicine* **18**(2), 309–319 (1991).
- [16] Reiter, A. and Bell, M. A. L., “A machine learning approach to identifying point source locations in photoacoustic data,” in [*Photons Plus Ultrasound: Imaging and Sensing 2017*], **10064**, 100643J, International Society for Optics and Photonics (2017).
- [17] Allman, D., Reiter, A., and Bell, M. A. L., “A machine learning method to identify and remove reflection artifacts in photoacoustic channel data,” *IEEE International Ultrasonics Symposium* (2017).
- [18] Allman, D., Reiter, A., and Bell, M. A. L., “Photoacoustic source detection and reflection artifact removal enabled by deep learning,” *IEEE Transactions on Medical Imaging* **37**(6), 1464–1477 (2018).
- [19] Nicholson, P., Haddaway, M., and Davie, M., “The dependence of ultrasonic properties on orientation in human vertebral bone,” *Physics in Medicine & Biology* **39**(6), 1013 (1994).
- [20] Medwin, H., “Speed of sound in water: A simple equation for realistic parameters,” *The Journal of the Acoustical Society of America* **58**(6), 1318–1319 (1975).